Nuclear Inst. and Methods in Physics Research, A 1027 (2022) 166253

Contents lists available at ScienceDirect

Nuclear Inst. and Methods in Physics Research, A

journal homepage: www.elsevier.com/locate/nima

Position sensitive plastic scintillator for beta particle detection

H. Joukainen *, J. Sarén, P. Ruotsalainen

University of Jyvaskyla, Department of Physics, P.O. Box 35, FI-40014 Jyvaskyla, Finland

ARTICLE INFO

Keywords:
Plastic scintillator
Recoil-beta tagging
Decay tagging

ABSTRACT

A new segmented plastic scintillator detector Tuike has been developed for recoil-beta tagging experiments at the Accelerator Laboratory of the University of Jyväskylä. The detector consists of individual plastic scintillator bars arranged in two orthogonal layers, and the scintillation light is detected using silicon photomultipliers. Performance of the new detector was tested using fusion-evaporation reaction ^{40}Ca(^{36}Ar, pn)^{74}Rb, and the results are discussed here. It was found that for beta particles seen in the main silicon detector, Tuike can tag high-energy beta particles with a 48(10)% efficiency. An energy calibration method using Compton edges of gamma ray transitions is described in the present work. Tuike was demonstrated to improve the sensitivity to identify weak fusion-evaporation channels associated with beta decays having high beta end-point energy, enabling nuclear structure studies along the N = Z line.

1. Introduction

Experimental studies of exotic nuclei, such as those residing near the proton drip-line, starts with creation of those nuclei utilizing a particle accelerator. This can be achieved using fusion-evaporation reaction. The compound nucleus created in such a reaction has a high excitation energy, which quickly decreases by emitting light particles such as protons, neutrons and alphas. As a result, a wide variety of nuclei are created through different evaporation channels. It often happens that the channel of interest has vanishingly small production cross section and is therefore difficult to detect from the midst of other stronger reaction channels. As a first step, in-flight separators are used to separate the primary beam from the reaction products. Additionally, the mass-over-charge or m/q-value can be obtained when using a recoil-mass spectrometer such as the Mass Analyzing Recoil Apparatus MARA [1] and used for further identification. Specific nucleus of interest can be identified based on its decay properties, and this procedure is called the recoil-decay tagging (RDT) method [2,3].

In RDT, the created nuclei of interest and radiation events related to them can be tagged by observing alpha or proton decays [4] or even isomeric gamma-rays [5] from the product at the focal plane of a recoil separator. A more recently developed extension of the RDT method is recoil-beta tagging (RBT), where beta particles are used as a tag. This is much more challenging in comparison to alpha and proton tagging, because beta decay is a three-body process and therefore the beta energy spectrum is continuous, making it difficult to resolve the origin of a beta particle. However, there exist cases where the beta decay properties are much more favorable for tagging purposes. Fermi superallowed beta decays have high beta decay end-point energies up to 10 MeV and relatively fast ground state decay half lives of the order of 100 ms. With these characteristics it is possible to employ the beta particles as a decay tag and distinguish the reaction products.

In practice, RBT is done by an effective ΔE–E telescope at the focal plane of a recoil separator. The first part (ΔE) identifies the fast beta decay event, and the second (full E) then makes the separation between low and high-energy beta particles. At the Accelerator Laboratory of the University of Jyväskylä (JYFL), a Double-Sided Silicon strip Detector (DSSD) at the focal plane of MARA is used as a ΔE detector. In this article, we present a new segmented plastic scintillator detector to detect the full energy of a beta particle originating from a decaying recoil nucleus. We have named this detector as *Tuike* from the Finnish word for scintillation. In the past, other plastic scintillators have been tested for this purpose at JYFL. In general, plastic scintillator detectors are used widely in nuclear physics for beta particle detection, see for example Refs. [6–8].

The RBT method was validated at JYFL using a planar germanium detector in tandem with DSSD [9]. Later, a plastic scintillator based phoswich detector was developed for beta-tagging purposes [10]. The latter detector had a cleaner beta selection, since it could better distinguish between different types of ionizing radiation based on pulse shape discrimination. It also had faster signals than the planar Ge detector. Tuike is a step forward from these designs. It conserves the characteristic fast signal of a plastic scintillator and the discrimination ability between different types of ionizing radiation. With the addition of segmentation within the plastic layers, one gains position information for each event and increased toleration against high counting rates.

* Corresponding author.
E-mail address: henna.m.joukainen@jyu.fi (H. Joukainen).

https://doi.org/10.1016/j.nima.2021.166253
Received 4 August 2021; Received in revised form 2 November 2021; Accepted 17 December 2021
Available online 29 December 2021

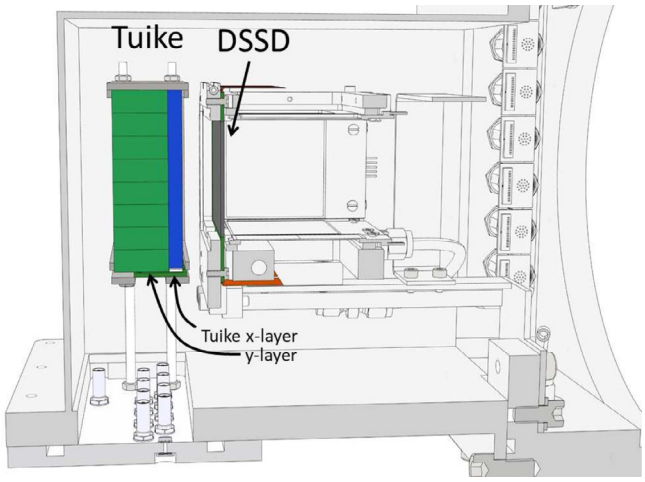

Fig. 1. Drawing of the focal plane chamber with Tuike (green and blue corresponding to y- and x-layer, respectively) and DSSD. In the picture, recoiling reaction products come in from the right. (For interpretation of the references to color in this figure legend, the reader is referred to the web version of this article.)

Realization of a compact, segmented scintillator detector such as Tuike has been made possible by recent advances in semiconductor technology leading to development of Silicon Photomultipliers (SiPM) [11]. Compared to traditional photomultiplier tubes, SiPMs are small, cost-effective and require voltages even less than 30 V. All the measurements presented here were carried out with operating voltage of 29 V in the SiPMs. Additionally, thanks to SiPMs, we no longer have to lead the light out of the vacuum chamber the detector resides in, but instead, only electric signals have to be transported out. SiPMs are also utilized in JYTube [12], a detector for prompt evaporated charged particles used at the MARA target area. SiPMs have truly opened new possibilities for more complex scintillator detector designs and for applications where position sensitivity is required such as in Tuike.

In this article, we describe the implementation and design principles of the new Tuike detector. We continue on describing the calibration process and present the results from performance tests and from a commissioning experiment. Lastly, we briefly discuss about the present status and future development plans of Tuike.

2. Detector design

2.1. Design principles

During the design phase, the new detector had two competing requirements: the detector has to be thick and wide enough for efficient beta particle detection but also small enough to have as little effect on the MARA focal plane gamma detectors as possible. Tuike resides at the MARA focal plane at 17 mm distance downstream from the DSSD detector, enclosed by a vacuum chamber made of aluminum (see Fig. 1). Typically four germanium detectors are installed on different sides around the chamber, one of which is behind Tuike.

A suitable thickness for Tuike was evaluated based on earlier beta-tagging experiments. As demonstrated in Ref. [9], for example, most of the detected beta particles appear below 5–6 MeV in the detector. The thicker the detector is, the wider is the maximum deposited energy range, but then the attenuation of the low-energy gamma rays increases. However, many of the beta particles arrive to the scintillator detector from DSSD in an angle, increasing the effective thickness. Additionally, the attenuation coefficient of plastic for gamma radiation is smaller in comparison to germanium. All beta particles recorded in Tuike having a higher energy than a given threshold set in analysis software are considered as high-energy betas, and therefore the minimum thickness of the detector is set by the highest expected energy threshold.

Table 1
Geometric efficiency ϵ_{geom} approximated at three different locations (marked on Fig. 2) for possible beta decay to end up impinging on Tuike. The values have been calculated for both front (at 17 mm distance) and back (at 17 + 30 mm) surfaces of Tuike using solid angles.

Position	Subtending surface	ϵ_{geom} (% of 4π)
(1)	Front	35
	Back	18
(2)	Front	31
	Back	9
(3)	Front	34
	Back	17
(4)	Front	23
	Back	12

In addition to the thickness, width and height of the scintillator detector have a direct effect on the gamma detectors' geometrical efficiency. Smaller detector allows use of a smaller vacuum chamber which minimizes the distance between the germanium detectors and the DSSD, where the recoils are implanted and emit isomeric gamma-ray transitions. However, it is still desirable to have the beta detector to cover at least the effective area of DSSD, so that any betas moving perpendicularly between the detectors are caught. With larger scintillator detector area, the detector subtends a larger solid angle with respect to DSSD and therefore its detection efficiency increases.

2.2. Description of the detector

With all the aforementioned design requirements in mind, Tuike's active dimensions are $140 \times 80 \times 30$ mm^3 (width, height and depth). Depth of 30 mm roughly corresponds to the CSDA (continuous slowing down approximation) range of 6 MeV beta particle in polyvinyltoluene (PVT) [13], where 6 MeV is expected to be the highest energy threshold required. Using the same approximation, beta particles of 7.0, 8.0 and 9.0 MeV will lose 5.5., 5.6 and 5.7 MeV in 30 mm of PVT, respectively. These were calculated using PVT thickness of 30 mm and density 1.023 g/cm^3. However, it bears repeating that more often than not the beta particles are going to hit the surface of Tuike in an angle and therefore experience thicknesses larger than 30 mm.

The geometry and dimensions of Tuike are illustrated in Fig. 2. The detector consists of two layers of scintillator bars which are placed orthogonally in such way that the first layer gives the x-coordinate and the second layer the y-coordinate. In the x-layer, the bars have dimensions of $10 \times 80 \times 6$ mm^3 while in the y-layer they are $140 \times 10 \times 24$ mm^3. Additionally, each bar has a frustum-shaped light guide on one end, with the top being 6×6 mm^2, matching the SiPM window size. The heights of the light guides are 2 mm for the x-layer and 9 mm for the y-layer. The scintillator material is Eljen technology's EJ-248 while the light guides are polymethyl methacrylate (PMMA). EJ-248's light yield is 60% of anthracene, decay time 2.1 ns and light attenuation length 250 cm [14]. For efficient light collection, the individual bars are covered with approximately 60 μm thick enhanced specular reflector (ESR) film manufactured by 3M, and the light guides are painted with Eljen's EJ-510 TiO_2 paint.

Width and height of Tuike were matched to those of the printed circuit board (PCB) of the DSSD. Taking into account only the positions of Tuike and DSSD and their active areas as seen in Fig. 2, the solid angle subtended by Tuike varies between 9%–35% depending on the position of the implanted recoil at DSSD and whether one uses the front or back surface of Tuike. Individual solid angle coverages for three different positions (marked in Fig. 2) are given in Table 1.

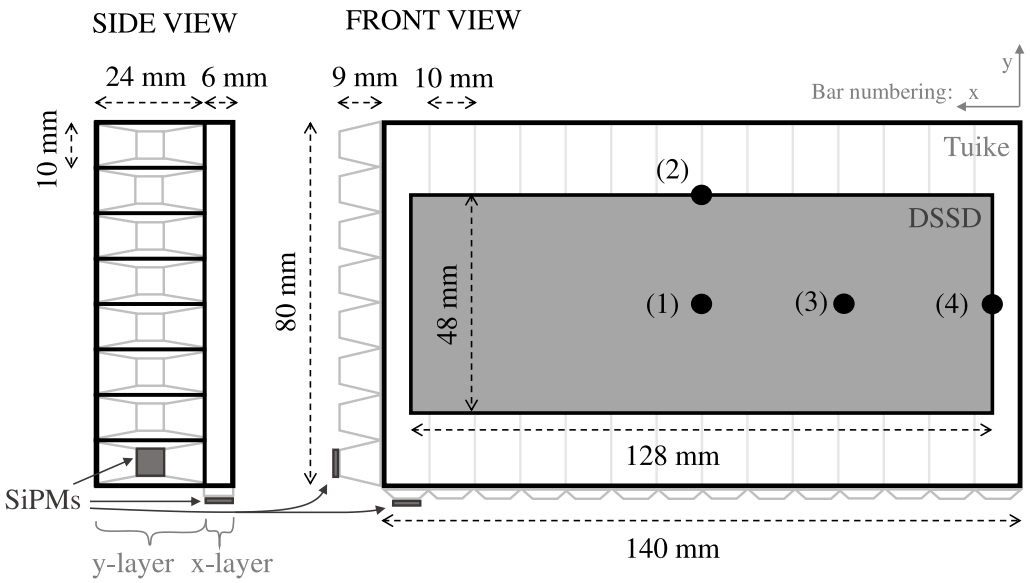

Fig. 2. Illustration of the geometry of Tuike from the front (right) and from one side (left) of the detector. Light guides are drawn with lighter color at the end of the bars. The SiPMs' PCBs have not been included in the figure. Active DSSD area (darker color) has also been marked to illustrate the relative positions of the two detectors. Numbers (1)–(4) correspond to points where the geometric detection efficiency has been evaluated in Table 1.

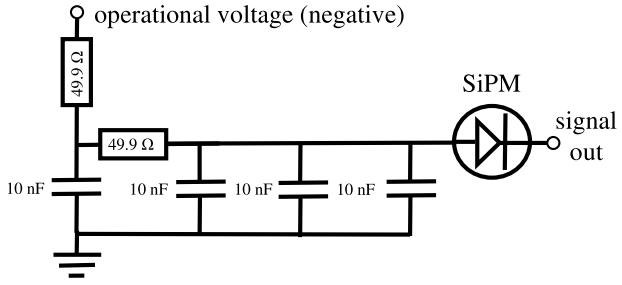

Fig. 3. Bias voltage filtering circuit attached to a SiPM. Each SiPM in Tuike has their bias voltage filtered individually.

Scintillation light is collected using C-series 6×6 mm^2 Silicon Photomultipliers (SiPM) manufactured by SensL (now ON Semiconductor). The size of a single microcell (consisting of a single photon avalanche diode and a quenching resistor) is 35×35 μm^2, and there are 18980 microcells in one SiPM. The breakdown voltage varies between 24.2 V and 24.7 V, and the recommended overvoltage range is 1.0–5.0 V. The maximum intensity wavelengths of the light emitted by the scintillators (425 nm) and the most sensitive wavelength region detected by the SiPMs (420 nm) match well. The SiPMs are mounted on individual PCBs housing a filtering circuit for the bias voltage. Circuit diagram of the bias filter is presented in Fig. 3. The design of the bias filter circuit was done before this project and is operationally similar to one proposed by the manufacturer. In the preliminary tests this configuration was found to be suitable for our use.

The PCBs have three connectors: one for the signal, one for the bias voltage, and one for grounding. All SiPMs are biased parallel inside the chamber and their signals are extracted separately through the vacuum chamber using Lemo feedthrough connectors. A special in-house designed differential driver circuit is then used to transform the signals into differential transfer lines of about 30 m. At the end of the line, the signals are transformed back into single-ended and fed into Nutaq ADCs with 100 MHz digitizers. The same interfaces are used by other auxiliary detectors in the measurement set-up, amounting up to 600 channels in total in the data acquisition system. Based on the gamma energy resolution and the low energy threshold achieved with germanium detectors, the signal transport chain has only a marginal effect on the results obtained with Tuike. All data acquisition channels are self-triggering and timestamped, i.e., the channels run independently and without a common trigger. The energy information of an event is determined by a gated integrator firmware running in the FPGA chips. For the results discussed in this paper, the signals were integrated for 3.2 μs starting from 110 ns before the trigger, while the baseline was averaged over a 160 ns window starting 630 ns before the trigger. Triggering is based on digital moving window deconvolution (MWD) algorithm [15], for which shaping time of 120 ns and decay constant of 3000 ns were used.

Both the ESR-foil and the SiPMs are attached to the scintillator bars using a Dow Corning Q2-3067 optical couplant, making them easily detachable in case of repair or if replacement parts are needed. It is not expected that Tuike will suffer from radiation damage. We have seen decreasing signal heights in a scintillator and SiPM combination caused by radiation damage at the target area, but Tuike is going to be used at the focal plane, where the dose rates are significantly lower. Additionally, Tuike is going to be used only for a few weeks a year, so the dose caused by background radiation is likely bigger than the one caused by experiments. No worsening of the vacuum has been observed when Tuike has been inserted into the focal plane vacuum chamber, which is usually operated at vacuum level of 10^{-5} hPa. As seen in Fig. 4, where the full detector is displayed, the scintillator bars and the SiPMs are further held together with a steel structure.

3. Calibration

Energy calibration of Tuike is based on observed Compton edges when known gamma-ray sources are used. Use of beta sources is not feasible, since the standard calibration sources have continuous energy spectra with low end-point energies, which makes the calibration of both x- and y-side difficult. Similarly, the conversion electrons from common electron sources have too low energies. In our case, sources containing ^{60}Co and ^{137}Cs were used for the calibration. The method of energy calibration of the individual channels, described in detail below, is adopted from Ref. [16]. After this, the summed energy spectra are adjusted to compensate for the light leakage between individual bars. This results in a calibration function for bar i from side j

$$E_{ij}(x) = A_{ij} B_j x, \tag{1}$$

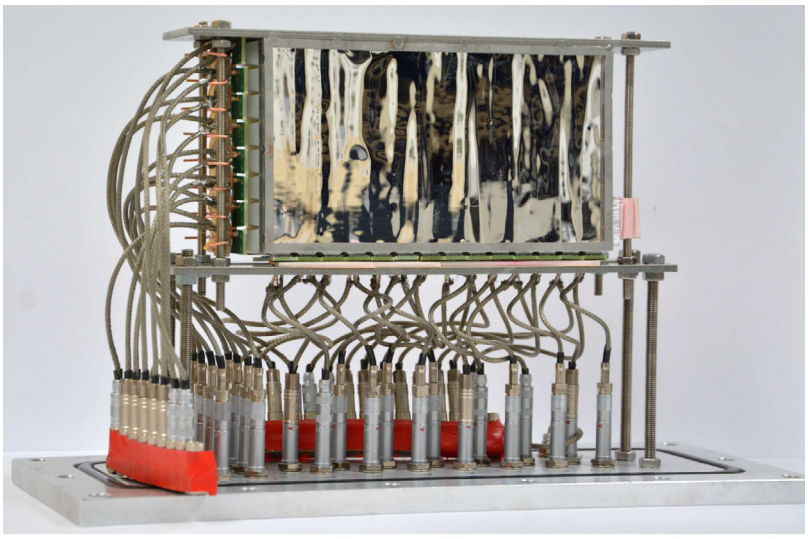

Fig. 4. Photograph of the full scintillator detector, Tuike. The striped pattern on the surface of Tuike is caused by the background reflecting off the slightly uneven surface covered by ESR foil.

where A_{ij} is the coefficient from the individual channel calibration, B_j is from the matching of summed energy spectra of x- and y-sides and x is the channel number. The two radiation sources were placed outside the vacuum chamber facing the y-layer of the detector and were measured separately. Because of the low Z of the constituents in plastic, the most probable interaction mechanism for gamma rays is Compton scattering. As an example, already at 40 keV, Compton scattering is about ten times more likely than the photoelectric absorption, while at 100 keV the ratio is 170 [17].

It was seen that for each scintillator bar, the Compton edges in the energy spectra had a similar kind of structure. We decided to use a sum of a Gaussian and a first order polynomial for the fit, from which the center of the Gaussian peak tells us the Compton maximum, i.e., the maximum point in a spectrum caused by Compton scattering. An example of the fit is in Fig. 5 using the ^{60}Co data from one scintillator bar. Using the maxima and the Compton edge to Compton maximum ratios determined in Ref. [16], the position of Compton edges in each bar can then be calculated. For ^{60}Co and ^{137}Cs the ratios are 0.96 and 0.88, respectively. Since the light production can be assumed to be directly proportional to the energy deposition of particles of same type into the scintillator, the energy calibration coefficients A_{ij} can be determined from a linear fit between calculated Compton edges against corresponding uncalibrated positions in the measured ^{60}Co and ^{137}Cs spectra. Typical shape of an energy spectrum of an individual x-layer detector can be seen in the panel (a) of Fig. 6.

It was observed that a scintillation event systematically causes a signal in the neighboring scintillator bars, which can be understood as a consequence of light leakage or secondary electrons crossing the scintillator boundaries. There is only one layer of ESR foil between the neighboring bars, attached with the optical couplant, and some small imperfections exist on the foil edges. Both of these may enable the light to propagate between the bars. The magnitudes of these two processes were studied by making a 2D histogram of relative signal amplitudes $(A_{i+1}/A_i, A_{i-1}/A_i)$ for detector i in cases where amplitude A_i was greater than both A_{i+1} and A_{i-1}. In panel (a) of Fig. 7, this is shown for x-layer scintillator number 4. The large locus containing most of the events is understood to represent physical events where the electron has not escaped to bars 3 and 5, and in this case, the signals in the neighboring bars are due to light leakage. The tails parallel to x- and y-axes are assumed to be caused by electrons that have escaped to corresponding neighbors. Furthermore, light was observed to be leaking even further away, which is evident in panel (b) of Fig. 7, showing relative amplitudes A_j/A_4 around detector 4. It can be observed that

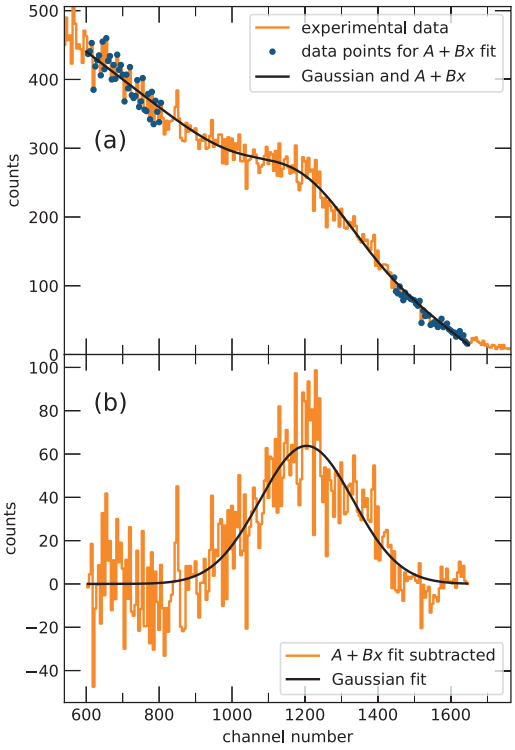

Fig. 5. Close-up to the Compton edge seen in one x-side scintillator bar using the ^{60}Co source. In panel (a) the whole data can be seen, with part of the data marked separately to show where the first order polynomial $(A + Bx)$ fit was made. In panel (b), the linear slope has been subtracted from the data and only the Gaussian fit is shown.

for this bar the signals in bars 3 and 5 are 22% and 28% of that in bar 4, respectively. Based on the distributions shown in the figure, the amount of light leakage is approximately constant for different events. It can also be seen that the amount of light leakage decreases exponentially as a function of distance. Other bars behave similarly in both layers. According to the data acquisition, time differences between signals originating from different bars seeing the same physical event are normally distributed with FWHM of roughly 20 ns.

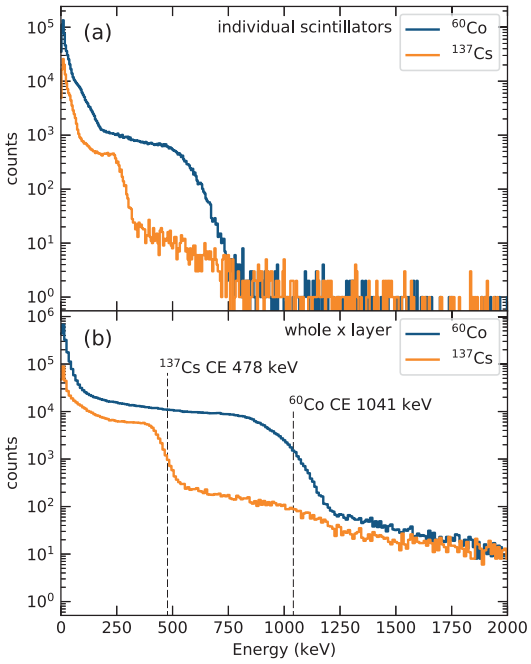

Fig. 6. Energy spectra of ^{60}Co and ^{137}Cs sources as measured with Tuike. (a) is from a single scintillator bar and (b) results from summing all x-layer energies during an event. The Compton edges (CE) in panel (a) appear at too low energies because part of the light is detected in the neighboring bars. The high-energy tails after the Compton edges are due to the background radiation and cosmic myons.

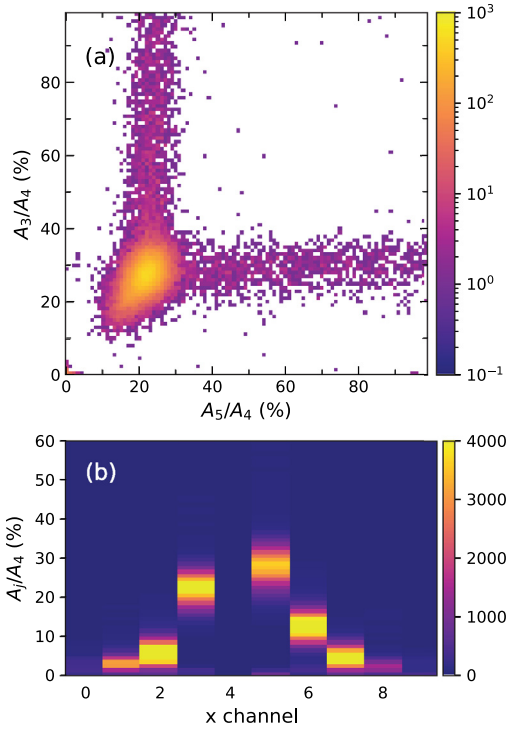

Fig. 7. Relative signal amplitudes in neighboring scintillator bars. In panel (a), signals in x-layer bar 4 are compared to signals in its two nearest neighbors, while in panel (b) the signal height is compared to the whole x-layer. Tails in panel (a) result from electrons that have interacted in the neighboring bars, while the bigger spot is due to the light leakage.

It was decided to sum up all signals separately in both x- and y-layer within 50-ns time window because we cannot easily distinguish for one event between light leakage and particle traveling in multiple bars. The light leakage between x- and y-layers were found to be negligible. To get the correct overall energies the calibration coefficients B_x and B_y for the sum spectra were first produced with the assumption that $B_j = 1$. These spectra were then scaled to find the correct values for B_x and B_y. The full energy of a particle is taken as a sum of energies from both x- and y-layer. The final energy spectra of the calibration sources are shown in Fig. 6b) for the x-layer.

4. Detector performance

Here, we showcase the ability to select high-energy betas with Tuike to enhance the sensitivity of interesting reaction channels using a known reaction ^{40}Ca(^{36}Ar, pn)^{74}Rb as a test. In addition to beta particles, this reaction produces highly-penetrating light particles, mainly protons, which are punching through the DSSD and stopped in the scintillator. The efficiency to detect these and scintillator response were measured. Additionally, as Tuike is part of a larger measurement system, including a gamma-ray detector behind the scintillator, the gamma ray transparency of the detector is an important property and hence was measured.

4.1. Beta tagging efficiency

The detector performance was tested in an experiment performed at JYFL using the K130 cyclotron to provide a beam for the fusion-evaporation reaction ^{40}Ca(^{36}Ar, pn)^{74}Rb with 103 MeV beam energy and a ^{nat}Ca target of thickness 0.75 mg/cm^2. Average beam intensity was 7.5 particle nano-amperes, i.e. the electrical current divided by the atomic charge state, and in total about 5 h of usable data were collected. ^{74}Rb decays by beta decay with 64.776(30) ms half-life and a high 10416.8(45) keV endpoint energy [18], making beta tagging of this nucleus possible. Additionally, its prompt low-energy gamma-ray energies are known, permitting investigation how the set beta energy threshold affects the available gamma-ray statistics. This same reaction was originally used in the proof-of-principle study of the RBT method using RITU separator and a planar germanium detector [9], further justifying the use of this reaction as a test for Tuike.

The vacuum-mode recoil separator MARA was used to separate the recoiling reaction products (“recoils”) from the primary ion beam. Prompt gamma rays were detected by the JUROGAM 3 spectrometer [19], which consists of 15 tapered coaxial and 24 clover high-purity germanium detectors. The charged particle detector JYTube was installed inside the target vacuum chamber, though it was not used in this analysis. At the focal plane of MARA, the recoils passed through a multi-wire proportional counter (MWPC) before being implanted into a double-sided silicon strip detector (DSSD) with a thickness of 300 μm. The time-of-flight between the MWPC and DSSD and the energy measured by the DSSD were used to differentiate between recoils and the scattered primary beam. Low-energy events observed by DSSD alone are classified as potential decays. Tuike was positioned right behind the DSSD as described earlier. All detector data were timestamped with a 100-MHz clock and recorded independently without a common trigger. The analysis was done using the GRAIN software package [20].

The position of recoils at the MARA focal plane depends on their mass-over-charge ratios. The focal plane is equipped with two sets of mass slits on both sides of the MWPC. In this test, two slits were set to allow two charge states of mass A=74 to enter the DSSD. This filters out most of the masses other than A=74, but due to the limited mass resolution of MARA, part of the other masses are still leaking through.

The fusion cross-section of ^{74}Rb is small compared to other evaporation channels and therefore its prompt gamma rays cannot be seen in a recoil-gated spectrum in panel (a) in Fig. 8, which consists of prompt gammas followed by a recoil detected at the focal plane within a time window representing the flight time over MARA. Adding the condition that a beta decay has been observed in the DSSD within a 200 ms time

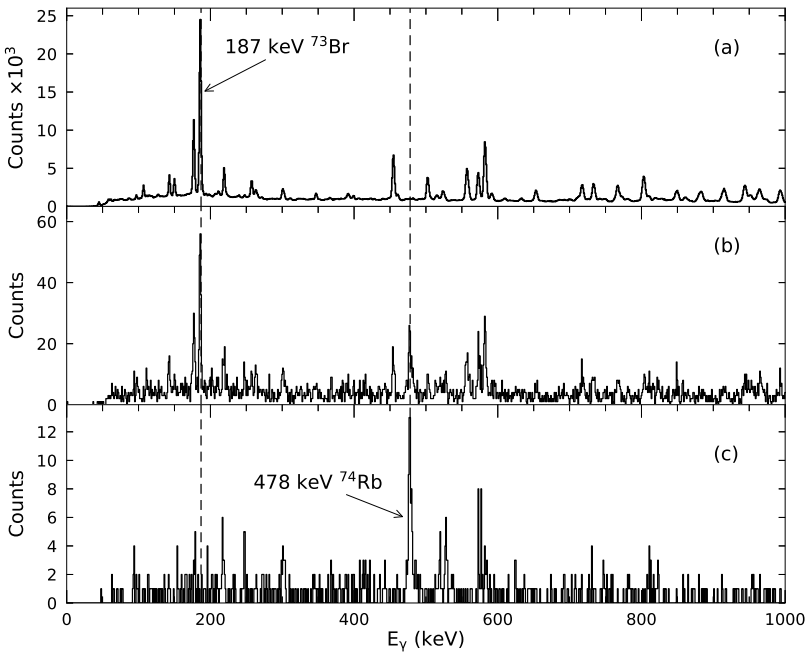

Fig. 8. Prompt gamma-ray spectra measured in reaction ^{40}Ca(^{36}Ar, pn)^{74}Rb with various gating conditions. (a) is recoil-gated, (b) recoil-gated with a decay observed within a 200 ms time window in the DSSD, and (c) recoil-gated with a 200 ms decay time window and requiring detection of a beta particle in Tuike with at least 3-MeV energy.

window after the recoil, the 478-keV peak from ^{74}Rb becomes clearly visible, as seen in panel (b) of the figure. However, the spectrum still contains quite large peaks originating from other stronger channels, such as ^{73}Br. Further requiring that Tuike has recorded a beta particle with energy over 3 MeV, the ^{74}Rb peak is even clearer and the main contaminant, 187-keV line from ^{73}Br fully disappears in panel (c).

As the beta end-point energy of ^{74}Rb is high compared to the neighboring nuclei produced in this reaction, this test reaction represents a typical experiment around the N=Z line where Tuike will be utilized. By increasing the energy threshold in Tuike, the amount of contaminants in the energy spectrum decreases and the ratio of events in the ^{74}Rb peaks in comparison to the contaminating lines increases. This was studied by examining the intensity ratio of the 478-keV transition in ^{74}Rb and the 187-keV transition in ^{73}Br as a function of the beta energy threshold. The results are presented in Fig. 9. Here, the correlation window between recoil and decay was lengthened to one second in order to increase statistics for the peak of the longer-lived ^{73}Br and improve this analysis. Normally, the shortest possible correlation time would be preferable. The decrease in statistics of ^{74}Rb as a function of beta energy threshold seen in the panel (a) of Fig. 9 shows the expected behavior caused by the beta energy distribution. Ratio of ^{73}Br to ^{74}Rb decreases rapidly with increasing threshold, and after 2 MeV the plot shows on average one randomly correlated ^{73}Br event to two events of ^{74}Rb in their corresponding peaks. Comparing the intensity of the ^{74}Rb 478-keV line using the 2 MeV energy threshold to the situation before tagging with Tuike (similar to panel (b) of Fig. 8), the resulting beta detection efficiency is 48(10)%. This number is larger than the estimated geometrical efficiency, because a beta leaves enough energy to be detected in the DSSD only if it is emitted to the hemisphere where Tuike is located. It is evident that while the statistics of the peak of interest decrease, with a careful choice of the energy threshold in Tuike, the contaminants can be removed efficiently while sufficiently conserving the peaks of interest.

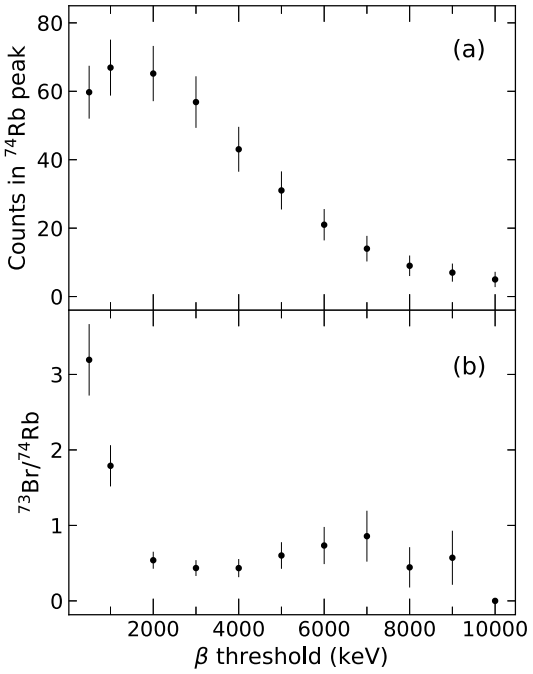

Fig. 9. Study of the effect of the beta energy threshold to the counts in the ^{74}Rb 478-keV peak (a) and to the ratio of the 478-keV to 187-keV transition of contaminant channel ^{73}Br (b).

4.2. Proton detection with tuike

It has been observed that there are light high-energy particles, typically alphas and protons produced in the bombarding process, entering the focal plane and punching through the DSSD. These are not registered by the MWPC due to low ionization of the filling gas, and therefore cannot be distinguished from decays at the DSSD. Tuike acting as a veto detector for these events was studied using ^{58}Ni beam at 228 MeV and ^{54}Fe target (0.763 mg/cm^2) with a gold backing. The focal plane set-up was the same as in the ^{74}Rb test.

Simultaneous energies measured by Tuike and the DSSD are shown in Fig. 10. Two separate groups are visible in the graph and they can be identified as beta particles and punch-through protons. Energy losses

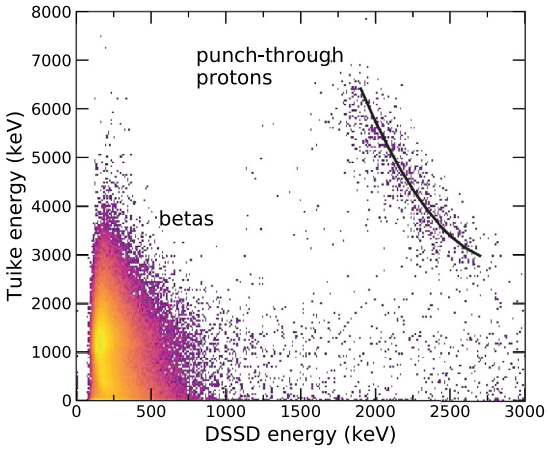

Fig. 10. Simultaneous energies measured in Tuike and DSSD. Two separate groups can be identified: beta particles and punch-through protons. A theoretical curve has been added to the proton group. Since the energy calibration of Tuike was made for electrons and the light output is different for electrons and protons, the proton energies appear to be about half of the real energy.

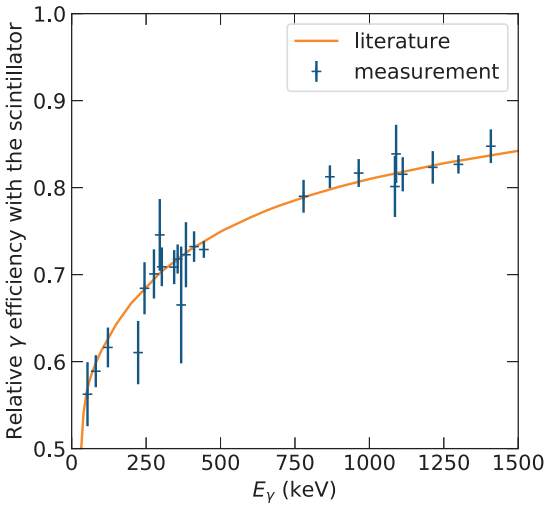

Fig. 11. Attenuation of gamma rays from a ^{155}Eu/^{133}Ba source through Tuike together with a calculated curve based on literature.

in 300 μm silicon were calculated for different proton energies and the remaining proton energies were determined using projected ranges calculated by SRIM [21]. Tuike calibration was made for electrons, and as light yield is less for protons, protons will appear lower in energy. In order to compare the observed punch-through events to the calculated values, light yield curves of electrons and protons [22] were utilized to determine corresponding electron energies in the plastic. The calculated curve and the observed events agree well with each other, also verifying the validity of the calibration. According to this analysis, protons arriving at the focal plane had energies of 11–15 MeV and they were entirely stopped in the scintillator after being slowed down in the DSSD to 8–13 MeV. It was also noted that Tuike detected nearly all punch-through proton events, meaning it can effectively work as a veto detector without the need to add an auxiliary detector between the DSSD and the scintillator and hence reduce the beta tagging efficiency of Tuike.

4.3. Gamma ray transparency

Even though Tuike is made of plastic, it still attenuates gamma rays, decreasing the efficiency of the germanium detector behind it. This effect was measured with a combined ^{155}Eu/^{133}Ba source attached to the center of the DSSD to mimic experimental conditions. The intensities of the gamma peaks were measured with and without the presence of Tuike, and their ratios are presented in Fig. 11. The ratios agree with values calculated with $I/I_0 = \exp[-(\mu/\rho)\rho x]$, where μ/ρ is the mass attenuation coefficient, ρ the density of the material and x the thickness. The mass attenuation coefficients for plastic scintillator were taken from Ref. [23], and for Tuike parameters $\rho = 1.023$ g/cm^3 and $x = 3.00$ cm were used. For typical gamma ray energies above 100 keV, the scintillator attenuates at most 40% of the gamma rays.

5. Conclusions and outlook

Performance of a new segmented scintillator detector Tuike for beta tagging experiments has been examined. According to the results presented here and the later experiments where this detector has been in use, the choices made during the designing phase are justified.

Calibration procedure for this detector is presented and it was found to be adequate to work as a beta tagging detector. Moreover, the calibration was found to be valid also for protons after correcting for different light yield. This result and the high geometrical efficiency for highly-energetic particles traveling through the focal plane enables Tuike to be used as a veto detector for punch-through proton events in the future.

The light leakage between neighboring bars was observed to be systematically around 20%–30%. This could have been decreased by adding more optical insulation between the scintillator bars, but the additional material would have slightly increased the inactive volume, which we wanted to minimize, and increased the complexity of the assembly. The presence of light leakage was predicted prior assembling the detector and we were anticipated to handle this by summing the neighboring signals in the data acquisition. It is possible that by characterizing the light leakage between every pair of bars and taking this into account in the calibration process will improve the energy resolution. However, this was deemed unnecessary in our case, especially since improvement is expected to be very small compared to the intrinsic energy resolution of the plastic scintillators.

In Tuike's current configuration, the scintillation light is detected by SiPMs, which are housed on separate circuit boards connected to two relatively rigid coaxial cables. While this configuration is fully operational, there are plans to modify the layout of biasing and signal circuits to decrease the volume these parts occupy. One solution could be to guide individual SiPM signals through a common PCB acting as a motherboard for small detachable biasing circuits. This would still allow small local adjustment of SiPMs to ensure good optical contact.

Tuike has successfully been used in three separate beta tagging experiments at the time of writing this article. While Tuike was designed for recoil-beta tagging, it can be used as a veto detector for focal plane beta particles as well, though this has not yet been tested in experimental conditions. So far, all testing and experiments have been done using the MARA recoil separator, but since the focal planes of both MARA and RITU [24] are identical, Tuike is likely to be used in RITU experiments in future as well.

CRediT authorship contribution statement

H. Joukainen: Conceptualization, methodology, investigation, Writing – original draft, Writing – review & editing, visualization. **J. Sarén:** Conceptualization, methodology, investigation, Writing – original draft, Writing – review & editing, project administration. **P. Ruotsalainen:** Writing – review & editing.

Declaration of competing interest

The authors declare that they have no known competing financial interests or personal relationships that could have appeared to influence the work reported in this paper.

Acknowledgments

Parts of this work were supported by the Academy of Finland under the Contract No. 213503 (Finnish Center of Excellence Programme). The authors are also grateful for the support of our local research group at the University of Jyväskylä.

References

[1] J. Uusitalo, J. Sarén, J. Partanen, J. Hilton, Mass analyzing recoil apparatus, MARA, Acta Phys. Polon. B 50 (3) (2019) 319–327, http://dx.doi.org/10.5506/APhysPolB.50.319.

[2] K.-H. Schmidt, R. Simon, J.-G. Keller, F. Hessberger, G. Münzenberg, B. Quint, H.-G. Clerc, W. Schwab, U. Gollerthan, C.-C. Sahm, Gamma-spectroscopic investigations in the radiative fusion reaction ^{90}Zr + ^{90}Zr, Phys. Lett. B 168 (1) (1986) 39–42, http://dx.doi.org/10.1016/0370-2693(86)91456-5.

[3] R.S. Simon, K.H. Schmidt, F.P. Heßberger, S. Hlavac, M. Honusek, G. Münzenberg, H.G. Clerc, U. Gollerthan, W. Schwab, Evidence for nuclear shape coexistence in ^{180}Hg, Z. Phys. A 325 (2) (1986) 197–202, http://dx.doi.org/10.1007/BF01289651.

[4] E.S. Paul, P.J. Woods, T. Davinson, R.D. Page, P.J. Sellin, C.W. Beausang, R.M. Clark, R.A. Cunningham, S.A. Forbes, D.B. Fossan, A. Gizon, J. Gizon, K. Hauschild, I.M. Hibbert, A.N. James, D.R. LaFosse, I. Lazarus, H. Schnare, J. Simpson, R. Wadsworth, M.P. Waring, In-beam γ-ray spectroscopy above ^{100}Sn using the new technique of recoil decay tagging, Phys. Rev. C 51 (1995) 78–87, http://dx.doi.org/10.1103/PhysRevC.51.78.

[5] D.M. Cullen, L.K. Pattison, R.S. Chakrawarthy, D. Dobson, J.L. Durell, S.J. Freeman, D.T. Scholes, C. Scholey, E.S. Paul, P.T.W. Choy, P.T. Greenlees, P.M. Jones, R. Julin, S. Juutinen, A. Keenan, H. Kettunen, P. Kuusiniemi, M. Leino, A.-P. Leppänen, P. Nieminen, J. Pakarinen, P. Rahkila, J. Uusitalo, M.A. Bentley, D.T. Joss, Identification of excited states in doubly odd $^{140}_{63}Eu_{77}$ by recoil-isomer tagging, Phys. Rev. C 66 (2002) 034308, http://dx.doi.org/10.1103/PhysRevC.66.034308.

[6] P.E. Garrett, C.E. Svensson, G.C. Ball, G. Hackman, E.F. Zganjar, C. Andreoiu, A. Andreyev, S.F. Ashley, R.A.E. Austin, D. Bandyopadhyay, J.A. Becker, S. Chan, H. Coombes, R. Churchman, R.S. Chakrawarthy, P. Finlay, G.F. Grinyer, B. Hyland, E. Illes, G.A. Jones, W.D. Kulp, J.R. Leslie, C. Mattoon, A.C. Morton, C.J. Pearson, A.A. Phillips, P.H. Regan, J.J. Ressler, F. Sarazin, M.A. Schumaker, J. Schwarzenberg, M.B. Smith, J.J. Valiente-Dobón, P.M. Walker, S.J. Williams, J.C. Waddington, L.M. Watters, J. Wong, J.L. Wood, Gamma-ray spectroscopy at TRIUMF-ISAC, AIP Conf. Proc. 819 (1) (2006) 249–253, http://dx.doi.org/10.1063/1.2187867.

[7] E.F. Zganjar, T. Achtzehn, D. Albers, C. Andereoiu, A.N. ANdreyev, R.A.E. Austin, G.C. Ball, J.A. Behr, G.C. Biosvert, Superallowed beta decay studies at TRIUMF — nuclear structure and fundamental symmetries, Acta Phys. Polon. B 38 (4) (2007) 1179–1194.

[8] D. Pauwels, O. Ivanov, J. Büscher, T. Cocolios, J. Gentens, M. Huyse, A. Korgul, Y. Kudryavtsev, R. Raabe, M. Sawicka, I. Stefanescu, J. Van de Walle, P. Van den Bergh, P. Van Duppen, Decay correlations in the seconds range with laser-ionized, mass-separated beams, Nucl. Instrum. Methods Phys. Res. B 266 (19) (2008) 4600–4605, http://dx.doi.org/10.1016/j.nimb.2008.05.083, Proceedings of the XVth International Conference on Electromagnetic Isotope Separators and Techniques Related to their Applications.

[9] A. Steer, D. Jenkins, R. Glover, B. Nara Singh, N. Pattabiraman, R. Wadsworth, S. Eeckhaudt, T. Grahn, P. Greenlees, P. Jones, R. Julin, S. Juutinen, M. Leino, M. Nyman, J. Pakarinen, P. Rahkila, J. Sarén, C. Scholey, J. Sorri, J. Uusitalo, P. Butler, I. Darby, R.-D. Herzberg, D. Joss, R. Page, J. Thomson, R. Lemmon, J. Simpson, B. Blank, Recoil-beta tagging: A novel technique for studying proton-drip-line nuclei, Nucl. Instrum. Methods Phys. Res. A 565 (2) (2006) 630–636, http://dx.doi.org/10.1016/j.nima.2006.06.034.

[10] J. Henderson, P. Ruotsalainen, D.G. Jenkins, C. Scholey, K. Auranen, P.J. Davies, T. Grahn, P.T. Greenlees, T.W. Henry, A. Herzáň, U. Jakobsson, P. Joshi, R. Julin, S. Juutinen, J. Konki, M. Leino, G. Lotay, A.J. Nichols, A. Obertelli, J. Pakarinen, J. Partanen, P. Peura, P. Rahkila, M. Sandzelius, J. Sarén, J. Sorri, S. Stolze, J. Uusitalo, R. Wadsworth, Enhancing the sensitivity of recoil-beta tagging, J. Instrum. 8 (04) (2013) P04025, http://dx.doi.org/10.1088/1748-0221/8/04/p04025.

[11] S. Gundacker, A. Heering, The silicon photomultiplier: fundamentals and applications of a modern solid-state photon detector, Phys. Med. Biol. 65 (17) (2020) 17TR01, http://dx.doi.org/10.1088/1361-6560/ab7b2d.

[12] P. Ruotsalainen, (unpublished).

[13] M.J. Berger, J.S. Coursey, M.A. Zucker, J. Chang, NIST standard reference database 124, 2017, http://dx.doi.org/10.18434/T4NC7P.

[14] Eljen Technology, High temperature EJ-244, EJ-248, EJ-244M, EJ-248M, 2021, https://eljentechnology.com/products/plastic-scintillators/ej-244-ej-248-ej-244m-ej-248m. (Accessed 19 October 2021).

[15] M. Lauer, Digital Signal Processing for Segmented HPGe Detectors, Preprocessing Algorithms and Pulse Shape Analysis (Ph.D. thesis), Ruperto-Carola University of Heidelberg, 2004.

[16] E. Siciliano, J. Ely, R. Kouzes, J. Schweppe, D. Strachan, S. Yokuda, Energy calibration of gamma spectra in plastic scintillators using compton kinematics, Nucl. Instrum. Methods Phys. Res. A 594 (2) (2008) 232–243, http://dx.doi.org/10.1016/j.nima.2008.06.031.

[17] M. Berger, J. Hubbell, S. Seltzer, J. Chang, J. Coursey, R. Sukumar, D. Zucker, K. Olsen, NIST standard reference database 8 (XGAM), 1998, http://dx.doi.org/10.18434/T48G6X.

[18] B. Singh, A.R. Farhan, Nuclear data sheets for A=74, Nucl. Data Sheets 107 (7) (2006) 1923–2102, http://dx.doi.org/10.1016/j.nds.2006.05.006.

[19] J. Pakarinen, J. Ojala, P. Ruotsalainen, H. Tann, H. Badran, T. Calverley, J. Hilton, T. Grahn, P.T. Greenlees, M. Hytönen, A. Illana, A. Kauppinen, M. Luoma, P. Papadakis, J. Partanen, K. Porras, M. Puskala, P. Rahkila, K. Ranttila, J. Sarén, M. Sandzelius, S. Szwec, J. Tuunanen, J. Uusitalo, G. Zimba, The JUROGAM 3 spectrometer, Eur. Phys. J. A 56 (2020) http://dx.doi.org/10.1140/epja/s10050-020-00144-6.

[20] P. Rahkila, Grain—A java data analysis system for total data readout, Nucl. Instrum. Methods Phys. Res. A 595 (3) (2008) 637–642, http://dx.doi.org/10.1016/j.nima.2008.08.039.

[21] J.F. Ziegler, M. Ziegler, J. Biersack, SRIM – the stopping and range of ions in matter (2010), Nucl. Instrum. Methods Phys. Res. B 268 (11) (2010) 1818–1823, http://dx.doi.org/10.1016/j.nimb.2010.02.091, 19th International Conference on Ion Beam Analysis.

[22] V. Verbinski, W. Burrus, T. Love, W. Zobel, N. Hill, R. Textor, Calibration of an organic scintillator for neutron spectrometry, Nucl. Instrum. Methods 65 (1) (1968) 8–25, http://dx.doi.org/10.1016/0029-554X(68)90003-7.

[23] J.H. Hubbell, S.M. Seltzer, NIST standard reference database 126, 1996, http://dx.doi.org/10.18434/T4D01F.

[24] J. Sarén, J. Uusitalo, M. Leino, J. Sorri, Absolute transmission and separation properties of the gas-filled recoil separator RITU, Nucl. Instrum. Methods Phys. Res. A 654 (1) (2011) 508–521, http://dx.doi.org/10.1016/j.nima.2011.06.068.